AGU ADVANCING EARTH AND SPACE SCIENCES

AGU Advances

RESEARCH ARTICLE
10.1029/2024AV001237

Peer Review The peer review history for this article is available as a PDF in the Supporting Information.

Key Points:

- We applied a multifrequency magnetic induction method to Galileo magnetometer observations at Callisto
- Joint assessment of flybys C03, C09, and C10 suggests that an ocean, and not an ionosphere alone, is required to explain the observations
- If an ocean is present, it is likely thick and deep

Supporting Information:

Supporting Information may be found in the online version of this article.

Correspondence to:

C. J. Cochrane,
corey.j.cochrane@jpl.nasa.gov

Citation:

Cochrane, C. J., Vance, S. D., Castillo-Rogez, J. C., Styczinski, M. J., & Liuzzo, L. (2025). Stronger evidence of a subsurface ocean within Callisto from a multifrequency investigation of its induced magnetic field. *AGU Advances*, *6*, e2024AV001237. https://doi.org/10.1029/2024AV001237

Received 3 MAR 2024
Accepted 7 JAN 2025

Author Contributions:

Conceptualization: Corey J. Cochrane
Data curation: Corey J. Cochrane, Steven D. Vance, Marshall J. Styczinski, Lucas Liuzzo
Formal analysis: Corey J. Cochrane, Lucas Liuzzo
Investigation: Corey J. Cochrane, Steven D. Vance, Julie C. Castillo-Rogez, Lucas Liuzzo
Methodology: Corey J. Cochrane, Lucas Liuzzo
Resources: Lucas Liuzzo

Stronger Evidence of a Subsurface Ocean Within Callisto From a Multifrequency Investigation of Its Induced Magnetic Field

Corey J. Cochrane[1], Steven D. Vance[1], Julie C. Castillo-Rogez[1], Marshall J. Styczinski[2], and Lucas Liuzzo[3]

[1]Jet Propulsion Laboratory, California Institute of Technology, Pasadena, CA, USA, [2]Blue Marble Space Institute of Science, Seattle, WA, USA, [3]Space Sciences Laboratory, University of California, Berkeley, CA, USA

Abstract The magnetometer investigation of the Galileo mission used the phenomenon of magnetic induction to produce the most compelling evidence that subsurface oceans exist within our solar system. Although there is high certainty that the induced field measured at Europa is attributed to a global-scale subsurface ocean, there is still uncertainty around the possibility that the induced field measured at Callisto is evidence of an ocean. This uncertainty is due to the presence of a conductive ionosphere, which will also produce an induction signal in response to Jupiter's strong time-varying magnetic field. Therefore, it is not yet known whether the observed induced field is attributable to the ionosphere, an ocean, or a combination of both. In this work, we use previously published simulations of Callisto's plasma interaction in combination with both an inverse and an ensemble forward modeling method to highlight the plausible range of interior properties of Callisto. We further constrain the ocean thickness and conductivity, ice shell thickness, and ionospheric conductivity that are required to explain the Galileo magnetometer observations. This is the first study to jointly consider all flybys to constrain the driving field and three flybys (C03, C09, and C10) to assess the induction response. Our results suggest that Callisto's response more likely arises from the combination of a thick conductive ocean and an ionosphere rather than from an ionosphere alone.

Plain Language Summary Magnetic measurements can tell us about the properties of subsurface oceans in moons, because oscillating magnetic fields from the planet interact with the electrically conductive ocean. Measuring the magnetic field near the moon can tell us about the ocean's properties, such as how deep it is and how much dissolved salt is present. Studies of magnetic measurements near Callisto, a large icy moon of Jupiter, have so far been ambiguous, because Callisto has a substantial ionosphere that may mimic the magnetic response of an ocean. However, past studies examining this problem considered only a subset of the available data. We expand the analysis to include data from a broader set of flybys from the Galileo mission, and when we include all of the available close flybys, we find that a deep ocean inside Callisto provides the most compelling explanation of the magnetic measurements.

1. Introduction

The Galileo spacecraft made eight low-altitude passes of Callisto (labeled C03, C09, C10, C20–23, C30) during its many orbits around Jupiter. Magnetic measurements near this large moon (radius of 2,410 km), obtained on each flyby except C20, provide a rich context for studying the surrounding space environment and moon–magnetosphere interactions. Oscillations in the magnetic field of Jupiter and its current sheet experienced by Callisto result in an apparent induced field that may imply the existence of an ocean (Zimmer et al., 2000). However, the weak induction signal (10's of nT, an order of magnitude weaker than Europa's), strong plasma influences, and unfavorable flyby geometries have resulted in ambiguity in the provenance of signals (Hartkorn & Saur, 2017; Liuzzo et al., 2016, 2017). Conditions at Callisto may also support a highly asymmetric ionosphere (Hartkorn et al., 2017), further complicating the interpretation of measurements (Styczinski et al., 2022). In this work, we combine advanced statistical techniques, models of contributions from the plasma environment, geophysical forward models constrained by gravity and bulk properties, and a detailed accounting of the excitation and possible induction fields from Callisto to determine whether the presence of an ocean is supported or refuted by the existing data.

Software: Corey J. Cochrane, Steven D. Vance, Marshall J. Styczinski
Supervision: Corey J. Cochrane
Visualization: Corey J. Cochrane, Marshall J. Styczinski
Writing – original draft: Corey J. Cochrane, Steven D. Vance, Julie C. Castillo-Rogez, Marshall J. Styczinski, Lucas Liuzzo
Writing – review & editing: Corey J. Cochrane, Steven D. Vance, Julie C. Castillo-Rogez, Marshall J. Styczinski, Lucas Liuzzo

Of the eight Galileo encounters of Callisto, only the magnetic field measurements obtained on C03 (4 November 1996, altitude 1139 km) and C09 (25 June 1997, altitude 421 km) are minimally affected by plasma interaction currents. As illustrated in Figure 1, these low-altitude measurements were made on the dawnside portion of Jupiter's magnetosphere, with Callisto located far from the center of the jovian current sheet. For this reason, the signatures of Callisto's induced field at these locations outside the current sheet are more discernible, since the magnitude of Jupiter's magnetospheric field near Callisto is maximized and currents associated with the moon's plasma interaction are minimized (see e.g., Figure 1 of Liuzzo et al., 2015). However, closer to the center of the sheet, the magnitude of the magnetospheric field decreases by more than an order of magnitude, while the density of the magnetospheric plasma increases. As such, the interaction between Callisto and its magnetospheric plasma environment generates strong perturbations to the local electromagnetic fields, obscuring the induction signature. During the C10 flyby (17 September 1997, altitude 538 km), Callisto was located closer to the center of the magnetospheric plasma sheet than during C03 or C09. As such, the data acquired during this encounter are not solely consistent with an induced dipole.

We note that magnetic latitude is an unreliable parameter for characterizing Callisto's plasma interaction strength on a flyby-to-flyby basis. For the orbital distance of Callisto, the Jovian magnetospheric field is not well represented by a dipole, and the variability near $26R_J$ causes significant deviations from the expected location of the magnetic equator of a dipole. Such an example of this occurred during the C23 and C30 encounters, which at distances of 1.08 and 3.50 R_J above the center of the magnetic dipole equator (see Liuzzo et al., 2015). However, magnetometer data from these encounters indicated crossings of the magnetic equator during these flybys as shown in Liuzzo et al. (2017). As such, the moon's plasma interaction during any specific encounter requires careful modeling of the electromagnetic field perturbations to accurately characterize the moon's perturbed magnetospheric environment, as is especially true when the flybys occur at the outskirts of the Jovian magnetospheric plasma sheet (e.g., during C10).

Measurements from the C21–C23 flybys cannot inform the interpretation of a global induction response, as these were all relatively high-altitude passes intended more for adjusting the spacecraft trajectory than for Callisto science. Each of the C21–C23 encounters was dominated by fields caused by magnetospheric plasma currents, which we term plasma interaction fields (PIFs). However, the data acquired from all of these flybys contain useful information about Jupiter's time-varying magnetic field and are therefore used in this study to assess the average driving field at Callisto. C22 was also far outside the plasma sheet, but the CA altitude for this flyby was nearly a full Callisto radius ($R_C = 2410.3\,\text{km}$) above the surface, so the signatures of the induced field were too weak to be measured due to the inverse distance cubed falloff of the response.

Using data from the C03 and C09 encounters, the initial analysis by Kivelson et al. (1999) confirmed that a global induced field was probably responsible for the response detected in the data, rather than a permanent intrinsic field. The follow-up analysis by Zimmer et al. (2000) modeled the induction response as a magnetic dipole with a dipole moment **M**,

$$\mathbf{M} = \Re\left\{-\frac{4\pi}{\mu_o}\frac{R_C^3}{2}Ae^{i\phi}\mathbf{B}_J(t)\right\} = -\frac{4\pi}{\mu_o}\frac{R_C^3}{2}\mathbf{m}(t), \tag{1}$$

in units of A m^2, where $\Re$ indicates the real part of the bracketed quantity, R_C is Callisto's radius, $\mathbf{B}_J(t)$ is Jupiter's driving field and $Ae^{i\phi}$ defines the complex response function of Callisto, with amplitude A and phase delay ϕ. $\mathbf{m}(t) = \Re\{Ae^{i\phi}\mathbf{B}_J(t)\}$ represents the time-varying portion of the induced magnetic moment, a scaled and time-delayed version of the driving field, with units of nT which results in the time-dependent magnetic field **B** defined by

$$\mathbf{B} = \frac{\mu_o}{4\pi}\frac{3(\mathbf{r}\cdot\mathbf{M})\mathbf{r} - |\mathbf{r}|^2\mathbf{M}}{|\mathbf{r}|^5}. \tag{2}$$

where **r** is the position relative to the center of Callisto. Zimmer et al. (2000) found that magnetic field flyby data acquired on C03 and C09 were consistent with an ocean with an induction amplitude in the range of $0.7 < A < 1$, irrespective of assumptions made about the phase lag. Zimmer et al. (2000) noted that because of uncertainties in the determination of the background field and perturbations from PIFs, it is difficult to constrain the parameter A

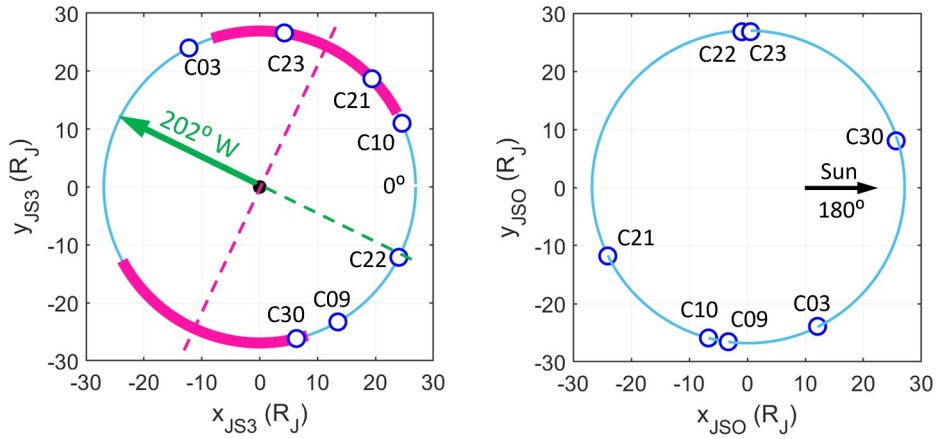

Figure 1. Characteristics of the low-altitude Galileo flybys of Callisto for which magnetic data are available. Left: The flyby orientation of Jupiter's magnetic field at closest approach (CA) in Jupiter System III (JS3) coordinates. The dotted green line represents the tilt direction of the magnetic dipole moment of Jupiter. The dotted red line represents the intersection of the magnetic equator of Jupiter with its equatorial plane, which is approximately where the plasma sheet crosses the plane of Callisto's orbit. The magenta arcs along the circle indicate the approximate extent of the plasma sheet, which we assume to be $2R_J$ thick. Right: Solar phase angle in the Jupiter–Sun–Orbit (JSO) reference frame to illustrate orbital phase coverage. A phase angle of zero (left edge) corresponds to when Callisto is opposite the Sun from Jupiter.

with better accuracy. These authors also noted that uncertainty in phase delay does not extend the range of possible amplitudes A beyond those estimated. The authors indicated that it is impossible to determine the phase delay from these data without better modeling of the magnetospheric environment and the moon–plasma interaction.

Subsequent analysis by Liuzzo et al. (2015, 2016) showed that the interaction between Callisto's ionosphere, the induced magnetic field, and the magnetospheric environment can generate strong perturbations to the local magnetic fields. These authors applied the hybrid model AIKEF (Adaptive Ion-Kinetic, Electron-Fluid; Müller et al., 2011) to constrain Callisto's plasma interaction. Studying the C03 and C09 Galileo encounters, (Liuzzo et al., 2015) assumed an amplitude of $A = 0.85$ with no phase delay to the inductive response, using the jovian magnetospheric background field at closest approach as the excitation field. They found that during these two flybys, Callisto's interaction with its magnetospheric plasma environment was weak; as a result, the magnetic field perturbations observed by Galileo during its encounters were consistent with the signatures of an induced field along the flyby trajectories (see also, e.g., Khurana et al., 1998; Kivelson et al., 1999; Zimmer et al., 2000). Note that the results from Liuzzo et al. (2015) for C03 and C09 did not include Callisto's atmosphere. However, since the plasma interaction currents during these two encounters were weak, this did not affect the authors' ability to explain the magnetic field signatures along the Galileo trajectory during these encounters. To confirm, we have investigated the magnetic field signatures from additional simulations that included the interaction with Callisto's atmosphere and found that the results do not differ by more than 10% from those in Liuzzo et al. (2015); we therefore proceed using their published results for this study. However, during the C10 encounter, the interaction between Jupiter's magnetospheric plasma and Callisto's atmosphere and induced field generated magnetic-field perturbations that obscured the "pure" signature of an inductive response (Liuzzo et al., 2016). Liuzzo et al. (2016) found that at distances greater than approximately $2R_C$, Callisto's plasma interaction generated magnetic field perturbations—field line pileup, draping, and Alfvén wings—that dominated the magnetic field signatures observed by Galileo. However, while located within the moon's geometric plasma shadow, Liuzzo et al. (2016) illustrated that the Galileo spacecraft detected magnetic field perturbations that were consistent with an induced field at the moon. These authors highlighted that induction signatures are clearly identifiable within the near-surface wakeside region that is "protected" from the moon's plasma interaction.

Further analysis of Galileo magnetometer data near Callisto by Hartkorn and Saur (2017) also demonstrated that while the induced magnetic signature could be attributed to magnetic induction originating from an ocean, the signatures are also consistent with the induction response from an ionosphere alone. These authors focused on modeling of inductive processes in Callisto's ionosphere and showed that the strength of response from ionospheric induction alone was comparable to a model consistent with the lower limit of the induced field suggested by Zimmer et al. (2000)—$A = 0.7$, with no phase delay ($\phi = 0°$). None of their ionospheric induction models

included the induced field from a possible ocean self-consistently, so their results suggest that ionospheric contributions are likely important, but the degree to which ionospheric induction is coupled with induction within an ocean remained uncertain.

Although the various assumptions made in the previous work were justified for the simulations carried out, some realities were not addressed. Callisto's actual response is anticipated to be driven at multiple frequencies—not just the 10.18 h synodic period—and therefore could have nonzero components of the induced magnetic moment at higher-order harmonics of the synodic, as suggested by the modeling performed in our work and by others (e.g., Seufert et al., 2011; Vance et al., 2021). Additionally, the majority of previous studies involving interpretation of Galileo measurements have assumed a single-frequency response that was scaled and perfectly synchronized with Jupiter's rotating field (i.e., zero phase delay), which is inconsistent with geophysical arguments of planetary bodies with multiple layers (including ionosphere) of varying levels of thickness and conductivity. The induction field is generally phase-delayed in time for a body with finite conductivity. Even if small, a phase-delayed induction response at the synodic period could leave room in the total induced response for a contribution from magnetic moments induced at other frequencies, as they will constructively and destructively interfere at different instants in time. Previous studies have also neglected to use the magnetic field measurements of the jovian field collected on the latter Galileo flybys of Callisto—namely C21, C22, C23, and C30—simply because they do not exhibit features consistent with an induced magnetic field. However, these flybys contain valuable information about Jupiter's driving field at Callisto for different solar phase angles and Jupiter System III longitudes (see Figure 1), and thus could be leveraged to better constrain Jupiter's driving field at Callisto and hence its induction response.

Here, we improve on previous studies by providing a more robust argument in favor of an ocean within Callisto by separating the induced field from the plasma contribution and then decomposing it using a multifrequency approach, exploiting the additional non-negligible harmonic external field components. Our results agree with previous studies that induction within an ionosphere is possibly consistent with the observed magnetic field signatures when analyzing data from flybys C03 and C09 alone. However, when including flyby C10, our results show that some combination of ionosphere and ocean is much more likely to be responsible for generating the magnetic field signatures that were measured by Galileo's magnetometer. While we provide further constraints on the range of likely interior properties of Callisto, it is not possible to uniquely constrain the moon's interior properties with the currently available data. This is due in particular to the uncertainty of the contributions of non-hydrostatic anomalies to the gravity data (Gao & Stevenson, 2013). However, future encounters (e.g., by Europa Clipper and JUICE) will help to further disentangle the information contained in geophysical signatures and derive definitive constraints on Callisto's interior.

2. Multi-Frequency Model of Jupiter's Driving Field

To infer Callisto's interior properties from the measurements acquired by Galileo, one must first understand the characteristics of Jupiter's driving field in Callisto's reference frame, since it is solely the dynamic external field that drives magnetic induction. Here, we not only use the data from flybys C03, C09, and C10 (which clearly exhibited induction signals), but we also use the magnetic measurements from flybys C21, C22, and C23 to better constrain the estimate of Jupiter's average driving field at Callisto, even though induction signals are not immediately detectable on these flybys, for reasons explained earlier.

Callisto and the other jovian moons experience slowly varying magnetic waves at multiple frequencies corresponding to Jupiter's apparent rotation period (10.18 h) and Callisto's orbital period (400 h). The former arises from the 9.6° tilt in Jupiter's magnetic axis with respect to its spin axis, and the latter arises from the spatial variation between the two bodies due to Callisto's slightly eccentric ($e = 0.0074$) and inclined orbit (0.19° with respect to the Laplace plane). Figure 2 illustrates the jovian magnetic field model of Khurana (1997). The top panel illustrates the magnetic field lines of Jupiter extending to Callisto's orbit, clearly showing the hinged equator and also the swept-back nature of the field lines in the insets of the panels, which affect the field magnitude and orientation at the position of Callisto, but not so much at the inner moons of Ganymede, Europa, and Io. The bottom panel of the figure illustrates the field response at Callisto as a function of frequency in the Callisto frame defined by the International Astronomical Union (IAU). In this frame, the x-axis is directed roughly toward Jupiter's center (oriented from Callisto's center to a specific surface feature on Callisto), the z-axis is parallel to Callisto's spin axis, and the y-axis completes the right-handed set (roughly opposite the orbital velocity). The IAU

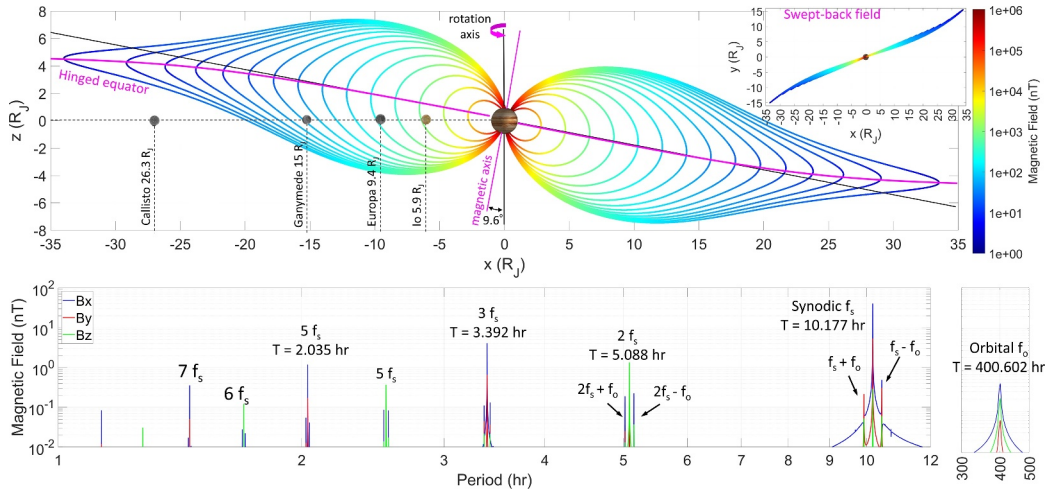

Figure 2. Jupiter magnetic field model evaluated at the position of Callisto in the moon's body-fixed IAU frame. Top: Field lines illustrated for the Khurana current sheet model, showing the orientation of the field at the orbit of Callisto from the hinged equator and in the swept-back nature of the field. Bottom: Frequency response at Callisto for the Khurana model, using the Voyager 2 parameter set noted in Table 1 of the publication.

frame (Archinal et al., 2018) is chosen for this work for convenience in implementation with SPICE and because it is a body-fixed frame, which is important for ocean induction. In the CPhiO frame often used in previous work, the x-axis is aligned with the direction of corotational flow, the z-axis is parallel to the jovian spin axis, and the y-axis completes the right-handed set (roughly toward Jupiter's center). Because Callisto's orbit has nonzero inclination and eccentricity, the CPhiO coordinate system varies over time with respect to a Callisto-fixed coordinate system. The CPhiO xy-plane is approximately a 90° rotation about the IAU z-axis of the IAU xy plane, and the z axes are nearly aligned, with these differences varying slightly throughout Callisto's orbit.

Note that there are very strong B_x and B_y components at the synodic period near Callisto, along with non-negligible 3rd (octupole) and 5th harmonics with B_z component at the synodic 2nd harmonic (quadrupole). Although the previous reports model the magnetic moment on each flyby assuming a driving field of zero in the vertical z direction (Hartkorn & Saur, 2017; Liuzzo et al., 2016; Zimmer et al., 2000), we account for a non-negligible component (of order 2 nT) as portrayed in the simulated models shown in Figure 2. Furthermore, solar-driven effects that are expected to cause magnetopause variability on the timescale of 641.9 h in the B_θ component may be present (Seufert et al., 2011), but we do not model magnetopause currents. This model provides information about the approximate amplitudes and phases of the waves that Callisto experiences, but more importantly, about the frequencies of those waves. Rather than using the amplitudes and phases of the waves from the models to infer the field at Callisto, we instead use the frequencies extracted from these models and solve for the amplitudes and phases directly using the Galileo magnetometer data. As will be discussed, we also use the more accurate (at the orbit of Callisto) current sheet model of Khurana (1997) to correct for differences in the field measured at the position of the Galileo spacecraft and that inferred at the position of Callisto.

As illustrated in Figure 2, it is clear that the field spectrum at Callisto can be represented by a superposition of magnetic waves at discrete frequencies corresponding to the 10.18 h synodic period, Callisto's 400.6 h orbital period, and the harmonics and beats of these two fundamental periods. The magnetospheric field of Jupiter at the position of Callisto $B_{J,C}$ can therefore be modeled in the frame of Callisto by a linear superposition of sinusoids,

$$\hat{\mathbf{B}}_{J,C}(t) = \sum_k \mathbf{B}_k \cos\left(2\pi f_k t + \theta_k\right) = \sum_k \mathbf{B}_{R,k} \cos\left(2\pi f_k t\right) + \mathbf{B}_{I,k} \sin\left(2\pi f_k t\right), \tag{3}$$

where t is time, $\mathbf{B}_{R,k} = \mathbf{B}_k \cos(\theta_k)$ and $\mathbf{B}_{I,k} = \mathbf{B}_k \sin(\theta_k)$. $\mathbf{B}_k = \left[B_{x,k}, B_{y,k}, B_{z,k}\right]$ are the amplitudes of the k^{th} discrete magnetic wave of Jupiter in the Callisto frame at frequency f_k and $\theta_k = \left[\theta_{x,k}, \theta_{y,k}, \theta_{z,k}\right]$ are their phases referenced with respect to the J2000 epoch. The parameter k ranges from $0 < k < K$, where $k = 0$ signifies $f_0 = 0$ Hz (DC) and K represents the number of frequencies to be modeled. Note that in this work, we use the

Table 1
List of Magnetic Field Coefficients (Referenced to the J2000 Epoch) in Units of nT for Dominant Waves From Khurana Spherical Harmonic Magnetic Field Model of Jupiter and the Sinusoidal Model Coefficients Obtained by Fitting Galileo Data From Callisto Passes C03, C09, C10, C21, C22, and C23

		Derived from spherical harmonic model (nT)								
	Period (hr)	$B_{x,R}$	$B_{x,I}$	$\lvert B_x\rvert$	$B_{y,R}$	$B_{y,I}$	$\lvert B_y\rvert$	$B_{z,R}$	$B_{z,I}$	$\lvert B_z\rvert$
f_S	10.177	−38.0	−6.8	38.6	3.7	0.6	3.79	−3.6	−3.8	5.28
$2f_S$	5.088	−0.2	0.2	0.34	−1.2	0.1	1.23	2.3	−0.4	2.6
$3f_S$	3.392	4.3	1.7	4.6	−1.3	0.1	1.3	−0.4	0.5	0.6
$5f_S$	2.035	−1.8	−0.02	1.8	0.30	−0.04	0.3	0.03	0.03	0.04
DC				−1.7			−1.2			−7.9
		Derived from Galileo flyby data (nT)								
	Period (hr)	$B_{x,R}$	$B_{x,I}$	$\lvert B_x\rvert$	$B_{y,R}$	$B_{y,I}$	$\lvert B_y\rvert$	$B_{z,R}$	$B_{z,I}$	$\lvert B_z\rvert$
f_S	10.177	−39.8	−3.2	39.9	0.5	5.85	5.87	0.8	−1.3	1.6
$2f_S$	5.088	−1.2	0.8	1.5	1.1	3.0	3.2	−2.2	−1.8	2.9
$3f_S$	3.392	7.27	0.5	7.29	1.8	0.6	1.88	0.1	−0.3	0.33
$5f_S$	2.035	−2.4	−0.5	2.46	0.3	−0.1	0.30	−0.2	0.3	0.34
DC				1.2			−3.5			−9.0

Note. Here, f_S represents the synodic period of Jupiter. Note that only a subset of frequencies were modeled as the small amplitude waves (<1 nT) cannot be accurately resolved with the limited amount of noisy measurements acquired by these flybys.

"hat" accent (e.g., $\hat{B}$) for estimations made from model and "tilde" accent (e.g., $\tilde{B}$) to refer to estimations made from data.

Table 1 illustrates the amplitude of each component for the dominant frequencies in the driving field, extracted from a spherical harmonic model-generated magnetic field time series spanning a 5-year period (4 August 1994–4 August 1999) using an unconstrained linear least-squares (LLS) approach. The method for obtaining these values is described in more detail elsewhere (Styczinski & Cochrane, 2024). Also included in the table are the amplitudes of each component obtained from inverting the Galileo measurements (i.e., C03, C09, C10, C21, C22, and C23), from a field-corrected data set. A correction to the data is required because the Galileo measurements do not represent the field at Callisto, but rather at the Galileo spacecraft. Because the Khurana (1997) model showed the best agreement with the data (using the Voyager 2 parameter set described in the publication) than the more recently developed Connerney et al. (2020) model, likely due to the model accounting for the effects of the hinging and the delay of the jovian current sheet exhibited at the orbit of Callisto, we use it to evaluate the magnetic field of Jupiter at the position of the spacecraft ($\mathbf{B}_{J,SC,m}$) and at the position of Callisto ($\mathbf{B}_{J,C,m}$). The correction, also used by Biersteker et al. (2023), Kivelson et al. (2023), and Cochrane et al. (2024), is defined by

$$\widetilde{\mathbf{B}}_{J,C}(t) \approx \mathbf{B}_{J,SC}(t) - \mathbf{B}_{J,SC,m}(t) + \mathbf{B}_{J,C,m}(t). \quad (4)$$

We model the DC, synodic, 2nd, 3rd, and 5th harmonic magnetic field components. In total, this yields two parameters for in-phase/out-of-phase (cos and sin dependence), ×3 parameters for each vector component, ×5 frequencies, plus three DC coefficients for a total of 27 Jupiter field model parameters. Note that we neglect the orbital component, as its amplitude is very small (<1 nT) and its effect on induction will be negligible, as the induction amplitude from an ocean at the long period of 400.6 h would be very small. The sum of squared errors are then minimized between $\widetilde{\mathbf{B}}_{J,C}(t)$ and $\hat{\mathbf{B}}_{J,C}(t)$ for all samples within ±1 hr duration around the closest approach of each flyby to acquire a set of driving field coefficients $B_{R,k}$ and $B_{I,k}$ that can then be used to further investigate Callisto's magnetic induction response. The magnitudes of these coefficients associated with this minimization are listed in the right column of Table 1 and the 6 panels of Figure 3 illustrate the comparison (blue, red, and green lines) between the field-corrected Galileo data set $\widetilde{\mathbf{B}}_{J,C}(t)$ and the multifrequency modeled field at Callisto $\hat{\mathbf{B}}_{J,C}(t)$ (black dotted lines) for the six Callisto flybys. The instantaneous driving fields at the closest approach time for the

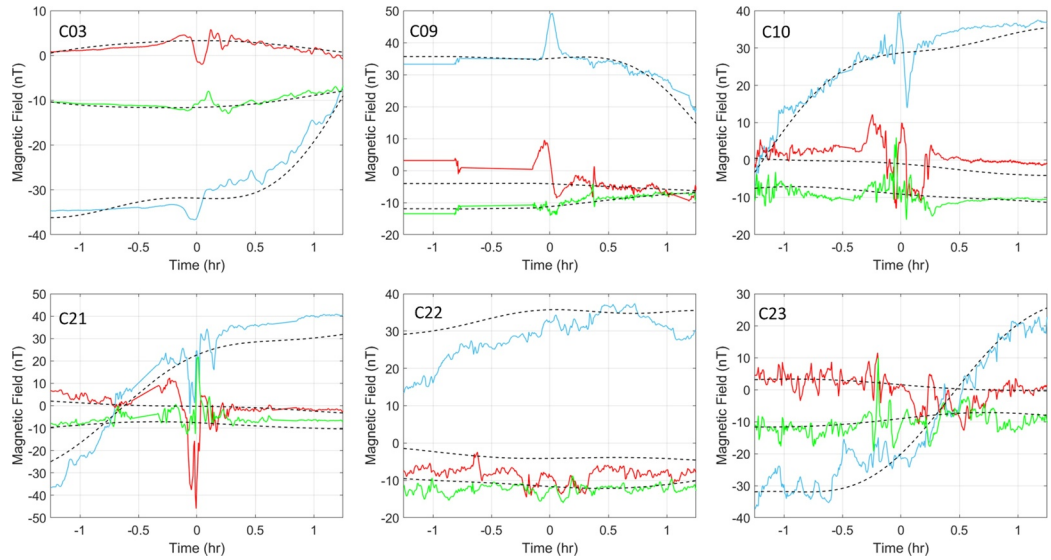

Figure 3. Field-corrected Galileo data obtained from Equation 4 (B_x is blue, B_y is red, and B_z is green in IAU body-centered Callisto frame) and the final multifrequency model, superimposed with black dotted lines plotted as a function of time with respect to closest approach to the moon.

three Callisto flybys are listed in Table 2 and compared with those reported in the literature that assumed a single frequency. Prior to using these coefficients for investigating Callisto's interior properties, the field contribution of the plasma currents must be first removed for each flyby which is the focus of the next section.

3. Removing Plasma Contribution From Callisto's Induction Response

Zimmer et al. (2000), Hartkorn and Saur (2017), and Liuzzo et al. (2015, 2016) each concluded that the local magnetic field in the vicinity of Callisto does not fit a perfect dipole response. Furthermore, Liuzzo et al. (2015, 2016, 2018) illustrated that any global induction signal may be partially obscured by magnetic perturbations caused by the moon's interaction with its local plasma environment. These hybrid kinetic model simulation studies assumed that the underlying induced dipole response was perfectly antialigned with the background inducing field (i.e., that Callisto is a perfectly conducting obstacle and therefore has no phase delay). For C03 and C09, these authors scaled the induction response to the *xy* driving field by 0.85, consistent with a highly saline ocean beneath an ice shell with appreciable thickness (see also Zimmer et al., 2000). For C10, they scaled the response by 1.0, consistent with a perfect conductor with Callisto's radius. However, these scaling configurations are not consistent across all flybys, they do not consider any potential phase delay in the synodic period (the presence of which would affect the measured induction amplitude), and they do not consider the additional contributions that occur at the higher-order harmonics that comprise the driving field environment.

Table 2
Instantaneous Evaluation of the Driving Field (i.e., Sum Over All Frequencies Except the DC Term) From Jupiter Used in Past Studies of the Induction Response of Callisto at the Time of Closest Approach (CA) for Flybys C03, C09, and C10

Instantaneous flyby driving field $B_x(t_{CA})$, $B_y(t_{CA})$, $B_z(t_{CA})$ (nT)					
Flyby	Sin. model derived from Khurana (1997)	Zimmer et al. (2000)	Liuzzo et al. (2015, 2016)	Hartkorn and Saur (2017)	This work
C03	−33.8, 5.0, −1.3	−31.7, 2.4, 0	−31.9, 2.4, 0	−31.1, 4.3, 0	−32.7, 6.6, −2.7
C09	35.5, −4.9, −1.6	33.7, −1.7, 0	33.6, −3.4, 0	35.2, −2.7, 0	33.8, −0.3, −2.1
C10	30.9, −2.2, 0.7	–	34.6, 0, 0	–	29.0, 2.84, −0.1

Note. Coordinates are in the IAU frame, to which past work has been converted from the CPhiO frame.

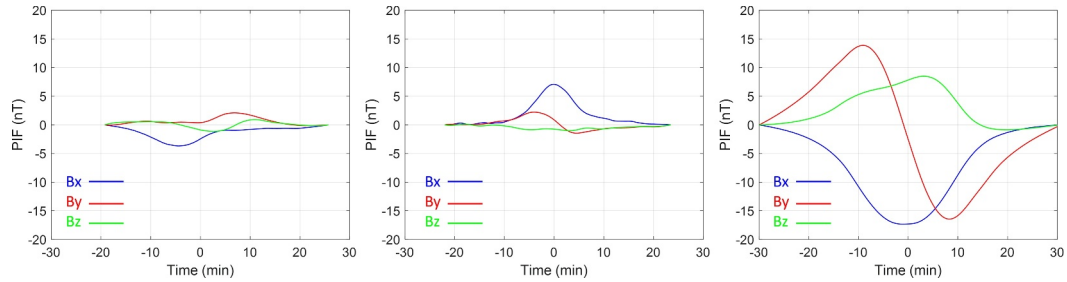

Figure 4. Plasma interaction fields for (left) C03 flyby, (middle) C09 flyby, and (right) C10 flyby. These time series represent the extracted structure of the plasma interaction field with Callisto, obtained by subtraction of the assumed induced dipole response from the hybrid kinetic magnetic field simulation performed by Liuzzo et al. (2015, 2016) and then baseline corrected.

In this section, we solve for the induced magnetic moment originating from Callisto's interior using a parameterized version of the plasma magnetic signatures simulated by Liuzzo et al. (2016) along each of the flybys. The magnetic signatures associated with Callisto's magnetospheric plasma interaction are visible in Figure 4, each computed by taking the difference between the total simulated magnetic field along the flyby obtained from hybrid kinetic modeling and the assumed underlying induced dipolar response, producing a structural "magnetic noise" time series consistent with the effect of the PIF for each of the flybys. As illustrated, during the upstream C09 encounter (middle panel), an enhanced magnetic field denoting the field line pileup is visible at a time near the closest approach of the moon (see also Figure A1 of Liuzzo et al., 2015). During the C10 encounter (right panel), the dipolar signature associated with field line draping/Alfvén wings is visible in the B_y component of the magnetic field along the Galileo trajectory (see also Figures 3 and 4 of Liuzzo et al., 2016). By including these noise signatures when inverting for the magnetic moment and parameterizing their scale factors, we can retain the inherent structure and features of the plasma noise inferred by the hybrid kinetic plasma modeling (e.g., magnetic field line pileup and Alfvén wing draping effects), which allows for a more accurate estimate of the induced magnetic moment that is buried in the data, one that is optimally different from a minimization perspective from the underlying moment used in the hybrid kinetic simulations of Liuzzo et al. (2015, 2016). Effectively, this minimization allows us to solve for the best estimate of M in the presence of the plasma source and does not restrict induction solely to the M_x and M_y components while also allowing the retention of an M_z component.

We performed separate inversions for each of the three flybys with noticeable induction signatures (C03, C09, C10) to isolate the magnetic moment from the scaled plasma signature and background jovian field. For each flyby, the total magnetic field at the position of the Galileo spacecraft B_{SC} is defined by

$$\mathbf{B}_{SC}(t) = \mathbf{B}_I(t) + \mathbf{B}_p(t) + \mathbf{B}_{J,SC}(t) + \mathbf{B}_n(t), \tag{5}$$

where $\mathbf{B}_I(t)$ represents the pure induction field contribution (from ocean, ionosphere, or both), $\mathbf{B}_p(t)$ represents the perturbation field present due to the plasma currents, $\mathbf{B}_{J,SC}(t)$ represents Jupiter's magnetic field at the position of the spacecraft, and $\mathbf{B}_n(t)$ represents the all other noise terms and small un-modeled effects. This field can be approximated with the following model:

$$\hat{\mathbf{B}}_{SC}(t) \approx \mathbf{D}(t)\mathbf{m} + C\mathbf{B}_p(t) + \mathbf{B}_O + \hat{\mathbf{B}}_{J,SC}(t), \tag{6}$$

where $\hat{\mathbf{B}}_{J,SC}(t)$ is the corrected background field model (similar to Equation 4) defined by

$$\hat{\mathbf{B}}_{J,SC}(t) = \hat{\mathbf{B}}_{J,C}(t) - \mathbf{B}_{J,C,m}(t) + \mathbf{B}_{J,SC,m}(t), \tag{7}$$

and $\mathbf{D}(t)\mathbf{m}$ is the induced magnetic field as a function of time with units of nT (essentially Equation 2 written in a different form) and $C\mathbf{B}_p(t)$ is the scaled plasma field component with offset $\mathbf{B}_O$. $\mathbf{B}_p(t)$ are the separated plasma field signatures for each flyby (i.e., dipole field subtracted from the total simulated field, shown in Figure 4 and obtained from Liuzzo et al. (2015, 2016)), and C is the plasma scale factor, assumed to be different for each flyby.

Table 3
Data Inversion Results for the C03, C09, and C10 Flybys of Callisto

Parameter	C03	C09	C10
$m = [m_x, m_y, m_z]$	$-25.8, 5.9, 2.8$	$27.8, 1.3, -3.0$	$29.8, 3.5, 2.4$
$\sigma_{m_x}, \sigma_{m_y}, \sigma_{m_z}$	0.7, 0.6, 1.3	0.6, 0.3, 0.6	1.5, 0.9, 2.0
$C(\sigma_C)$	0.69(0.05)	0.67(0.04)	0.45(0.02)

Note. Here are shown the values for the extracted magnetic moments and plasma scale factors with their 1σ standard deviation uncertainties, $\sigma_{m_{xyz}}$ and σ_C.

Although, a separate scale factor could be assigned to each axis for our purposes of mathematically extracting the optimal dipole signature, we instead constrain C to be equal to reduce degeneracy of the estimation and maintain a divergence-free vector field (i.e., $\nabla \mathbf{B} = 0$). $\mathbf{m} = [m_x, m_y, m_z]$ is the time-varying portion of the three-element induced dipole magnetic moment $\mathbf{M}$ with units of nT, assumed to be constant for the duration of the flyby and different for each flyby. $\mathbf{D}(t)$ is the dipolar matrix, defined by

$$\mathbf{D}(t) = -\frac{R_C^3}{2}\frac{1}{r(t)^5}\begin{bmatrix} 3x(t)^2 - r(t)^2 & 3x(t)y(t) & 3x(t)z(t) \\ 3y(t)x(t) & 3y(t)^2 - r(t)^2 & 3y(t)z(t) \\ 3z(t)x(t) & 3z(t)y(t) & 3z(t)^2 - r(t)^2 \end{bmatrix}, \quad (8)$$

where $x(t)$, $y(t)$, and $z(t)$ define the position of the spacecraft with respect to Callisto's center at each time t. We minimize the sum of squared errors between $\mathbf{B}_{SC}(t)$ and $\hat{\mathbf{B}}_{SC}(t)$ for each flyby separately to acquire a set of C and $\mathbf{m}$ for each of the flybys C03, C09, and C10. We use a constrained least squares method, restricting the scale factors to be within ± 2 and the induced magnetic moment vector within $[\pm 50nT, \pm 10nT, \pm 5nT]$, to significantly reduce the number of possible solutions that are able to fit the data. The parameters that were extracted are shown in Table 3 for each of the three flybys, along with their 1σ parameter uncertainties extracted from a derived covariance matrix. Differences in the values of the extracted moment (Table 3) from those of the driving field values (Table 2) are attributed to the scale factors and delays created by the imperfectly conducting interior. In subsequent sections, we use the isolated magnetic moments extracted here to further investigate the interior properties of Callisto.

We acknowledge that there are some uncertainties associated with the assumptions made in this approach. The properties of the magnetospheric plasma upstream of Callisto's environment were not well constrained by the Galileo spacecraft on a flyby-to-flyby basis. Furthermore, the properties of any conductive layers at Callisto (i.e., its ionosphere and a potential subsurface ocean), including their structure, composition, and conductivity profiles, were not well constrained so assumptions were made about the strength of the induced dipole used for the plasma simulations. Additionally, only the C10 flyby was modeled with a self-consistent conducting ionosphere in addition to the currents generated by Callisto's plasma interaction. As a result, there are uncertainties in the magnetic field perturbations detected along a spacecraft trajectory that are associated with Callisto's magnetospheric plasma interaction. For example, differences between the upstream density applied by Liuzzo et al. (2016) in their model and the true value during the C10 encounter would cause minor differences in the magnetic field strength along the Galileo trajectory (see Figure 3). In addition, asymmetries in the structure of Callisto's ionosphere would generate a nondipolar component to Callisto's inductive response, which was not included in the model of Liuzzo et al. (2015, 2016). This change in the inductive response couples nonlinearly to the structures associated with Callisto's plasma interaction, for example, the Alfvén wings (see Neubauer, 1999). However, even though the plasma signatures generated in the hybrid kinetic model are approximate, they are likely to resemble the real magnetic signatures (e.g., magnetic field line pileup and Alfvén wing draping effects) and our scaling allows for correction of quantitative differences. We also caution the reader that the effects of asymmetries would slightly alter the analysis, but would not greatly affect our conclusions (see Section 5.2) Despite these uncertainties and assumptions, the novel approach introduced in this work best constrains the properties of Callisto's inductive response using magnetic field data from the Galileo mission alone. We stress that future data sets obtained by Europa Clipper and JUICE will place further constraints on Callisto's ocean, conducting ionosphere, and magnetospheric plasma environment.

4. Assessment of Callisto's Interior Properties

With the driving field parameters in hand, we now assess the estimated dipole magnetic moments retrieved from the last section, free of plasma signatures, using two different methods. The first method entails comparing the moments to a large ensemble of forward models and the second is based on data inversion. The forward modeling approach is more ideal in the case of analyzing the limited set of Galileo observations because of its ability to automatically provide constraints on the interior properties of the ocean and ionosphere. As will be shown, a

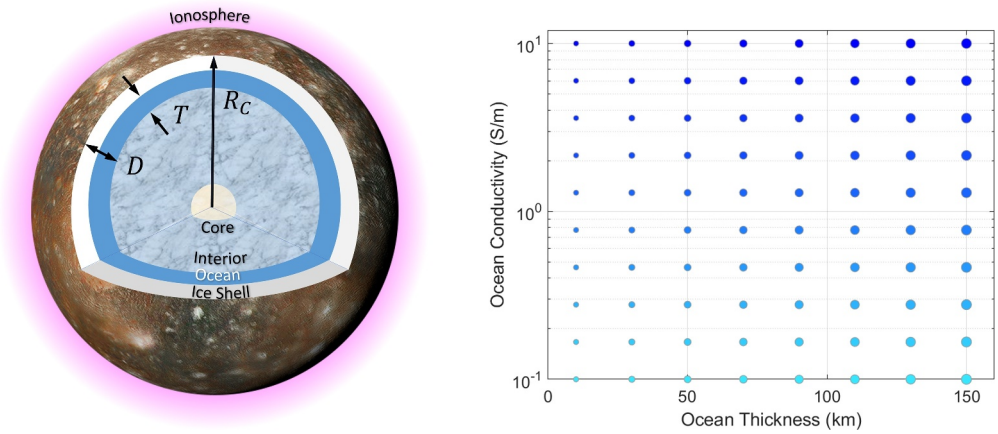

Figure 5. Forward model parameter space for ocean plus ionosphere models. Left: Schematic diagram of the 4-layer interior model of Callisto, consisting of a non-conductive mantle, a conductive ocean, a non-conductive ice-shell, and a conductive ionosphere. Right: Ocean parameter space used in this study, with eight linear steps of 20 km in ocean thickness T (10–150 km and also including the no ocean case when $T = 0$) and 10 uniform steps in log space for ocean conductivity σ (0.1–10.0 S/m). This parameter space was evaluated for six different seafloor depths D (130, 170, 210, 250, 290, 330 km), then each of these were convolved with ionospheres across 51 uniform log steps in conductance, totaling more than 24 thousand combinations.

multi-frequency data inversion method can also be used in conjunction with the forward modeling approach to classify the estimated response at the synodic period; however, further constraining interior properties remains difficult as it is nearly impossible to constrain the high order harmonics as will be shown.

In the forward modeling approach, the range of plausible interior properties that Callisto may possess can be determined by finding the subset of models in the forward model set that best fits the extracted magnetic moments (Table 3), thus determining whether the induction response originates from an ionosphere, an ocean, or a combination of both. A similar approach was previously used to classify magnetic moments for the moons of Uranus (Cochrane et al., 2021) and the principal components (PC) of the magnetic field data for Neptune's moon Triton (Cochrane et al., 2022). We use a similar ensemble modeling approach; however, here the classification space is in the complex response domain of the synodic period, where there is a clear clustering of similar-model classes. Like the magnetic moment and PC spaces, this classification space can be easily increased in dimensionality to enhance characterization robustness if parameters associated with different periods were used.

We use the open-source software frameworks *PlanetProfile* (Styczinski, Vance, Niesyt, et al., 2023; Vance et al., 2021) and *MoonMag* (Styczinski, 2024; Styczinski et al., 2022) to compute the complex response function (i.e., amplitudes A_k and phases ϕ_k) associated with more than 24 thousand different forward model configurations for Callisto's interior structure. The analytical solution to the complex response function was first derived by Srivastava (1966), and used by others (Biersteker et al., 2023; Khurana et al., 2002; Seufert et al., 2011; Zimmer et al., 2000) to model magnetic induction using a three-layer interior model (e.g., conductive ocean with non-conductive ice and mantle layers). *PlanetProfile* conversely leverages a numerical solution to calculate the complex response function from an arbitrary number of layers (Eckhardt, 1963). We use the optimized numerical solution, derived in the supplement of Vance et al. (2021), to calculate a 4-layer model which includes an upper layer representing the conducting ionosphere.

Among these models, we vary the thickness of the ice shell, the thickness T of the ocean (10–150 km), and the conductivity σ ((0.1–10.0 S/m), assumed to be uniform) as shown in Figure 5 (right). In addition, we vary the depth D of the seafloor (130–330 km) and also the ionospheric conductance (which we call the height-integrated conductivity, HIC) with an assumed extent of 100 km above the surface. Although radio occultation measurements made by Galileo provide valuable insight into the conductivity Callisto's ionosphere, we do not limit our models to reflect these measurements as they represent the local measure of the electron density and scale height of the ionosphere. Rather than forcing a parameter that doesn't necessarily reflect the effective global ionospheric conductance, we allow it to vary in our models to determine the range of ionospheric HIC that fit the observations due to the global uncertainty of this parameter.

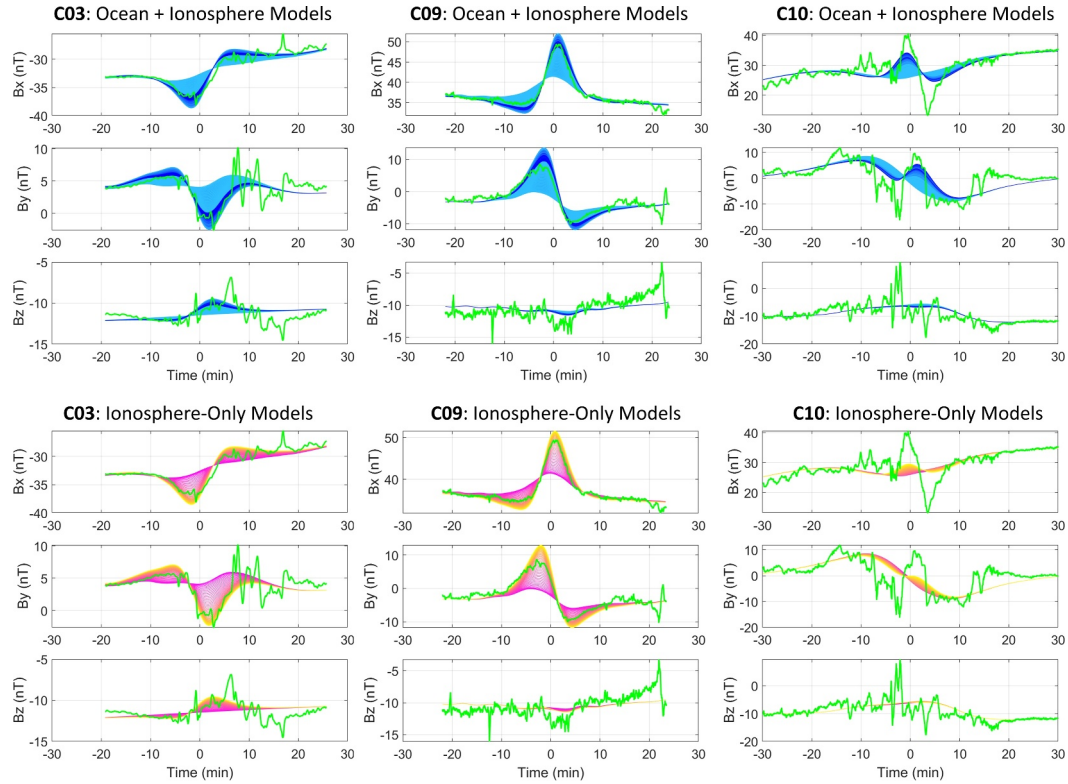

Figure 6. The magnetic induction response associated with all forward models in our study plotted against the Galileo magnetometer measurements in green. The top row of images illustrate the response associated with the ocean-plus-ionosphere models while the bottom row of images illustrate response associated with the ionosphere-only models. Note that the coloring scheme of the model responses is consistent with the other figures in the manuscript.

We calculate the complex response function for a wide range of frequencies (10^{-2} to 10^{4} Hz) for all models in the ensemble (see Figure S1 in Supporting Information S1). Using the amplitudes and phase delays of these models at the frequencies of interest (Table 1, peaks in Figure 2), we forward model the induced dipole response along the trajectory of the Galileo flybys of Callisto using Equation 2 while using the planetary field coefficients that were extracted from the Galileo measurements shown in Table 1. The induced dipole responses for all models are plotted in Figure 6 to show the wide range of possible responses of the entire data set. The figure qualitatively illustrates that although both a variety of ocean-plus-ionosphere models and ionosphere-only models can replicate the observations made on C03 and C09, an ocean-plus-ionosphere model is much more likely to replicate the observations made on flyby C10, simply from visual inspection. The goal now is to determine whether these same ocean models are able to also reproduce the signatures in flybys C03 and C09.

Because it is nearly impossible to visually make inferences on the measurements when plotted in the time domain without any data processing, especially jointly across the three flybys, we move to the synodic complex plane, ($A_k cos(\phi_k)$ versus $A_k sin(\phi_k)$, where k is associated with the frequency) illustrated in Figure 7. In the top panel, the colors of the ocean + ionosphere models (dots with blue shading) are based on the ocean conductivity, whereas the colors of the ionosphere-only models (dots with magenta-to-yellow shading) are based on ionospheric HIC. Unlike the plots in Figure 6, the clustering behavior of similar models in the synodic complex domain shown here is very convenient for characterization, as it allows distinguishability between ocean + ionosphere and ionosphere-only model classes. In the bottom left and right panels of the figure, the models are again plotted in the synodic complex domain, but colored according to the root mean squared error (RMSE) computed between their forward-modeled dipole responses (i.e., Figure 6) and the induced dipole responses estimated from the Galileo measurements on each flyby (±25 min of closest approach). Note that the RMSE in this case is therefore a relative measure of similarity, thereby facilitating the identification of the range of forward-modeled ocean cases that are more likely to explain the observations from the ensemble across all three flybys. The bottom left panel represents the RMSEs obtained for the two-flyby case (C03, C09) and the

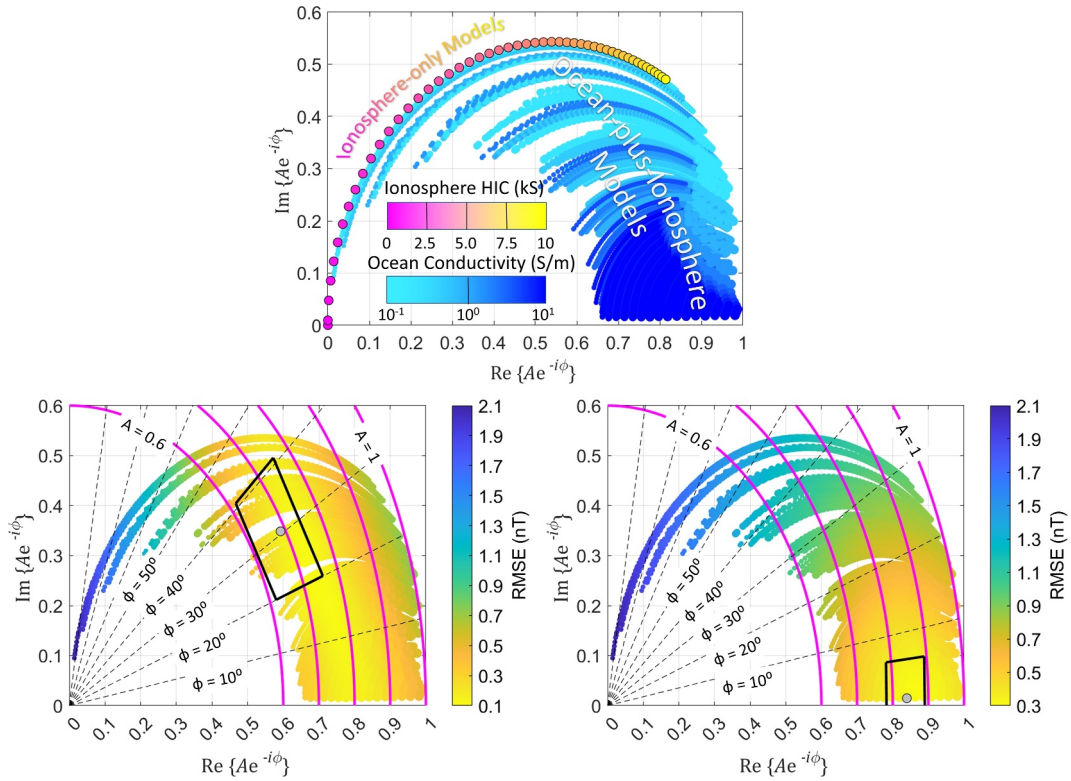

Figure 7. Top: Complex responses for all 24k models evaluated at the synodic period. Color and sizing scheme of forward models are consistent with that used in Figure 5: shades of blue dots represent the ocean-plus-ionosphere models colored according to their ocean conductivity and shades of yellow–magenta dots represent ionosphere-only models (i.e., no ocean), colored according to their ionospheric conductance. Bottom Left: The complex response for all forward models, colored coded by the root-mean-squared error (RMSE) difference between each forward model and the jointly modeled observations from the C03 and C09 flybys (e.g., $\mathbf{D}(t)\mathbf{m}$ from Equation 6), with best fit model exhibiting an RMSE of 0.13 nT. Bottom Right: A similar plot when using the jointly modeled observations from the C03, C09, and C10 flybys, with best fit model exhibiting an RMSE of 0.32 nT. Note that the single gray dot in each plot illustrates the estimate of the synodic parameters when using joint-flyby data inversion scheme. The bounding black quadrilateral defines the associated 3-sigma confidence interval for the estimated synodic parameters. Note that both methods are consistent in producing similar conclusions when either two or three flybys are used.

bottom right panel represents the RMSEs obtained for the three-flyby case (C03, C09, C10). Models with smaller errors indicate more similarity to the observations. It's clear from the two flyby case that the lowest RMSE models (bright yellow dots) lie both near the ionosphere-only boundary of models and also far from them, suggesting the observations from these two flybys alone are insufficient for ocean existence determination. However, in the three-flyby case, the presence of an ocean is favored when C10 is retained in the analysis, as the forward models with lowest RMSE are located farther from the ionosphere-only boundary of models in the synodic space, with most similar models with amplitude ranging from 0.75 to 0.95 and phase delay of <10deg.

Also plotted in the bottom left and right panels of Figure 7 are the estimated complex parameters of the synodic period and their associated confidence intervals, acquired using a joint-flyby multi-frequency inversion approach, for the two and three flyby cases. Note that the locations of each of these estimates (gray dots) lie in locations that are consistent with the cluster of forward models with lowest RMSEs for each case. In this inversion approach, we use a constrained nonlinear least-squares (NLLS) solver (e.g., Levenberg–Marquardt) to minimize the following function with respect to A_k and ϕ_k for all samples in time t for two cases—(1) using two flybys F = C03 and C09 and (2) using three flybys F = C03, C09, and C10:

$$\arg\min_{A_k,\phi_k} \sum_F \sum_t (\mathbf{D}_F(t)\mathbf{m}_F - \mathbf{D}_F(t)\hat{\mathbf{m}}(t))^2, \quad (9)$$

Table 4
Parameters Acquired From Multi-Frequency Inversion of Callisto's Induction Response Across Two (C03, C09) and Three (C03, C09, C10) Flybys, With Their Associated Uncertainties, $\sigma_{|A|}$ and σ_{phi} (One Standard Deviation)

Label	Period (h)	$\lvert A\rvert(\sigma_{\lvert A\rvert})$	$\phi(^\circ)(\sigma_\phi)$	A_R	A_I
Inverted parameters using data from flybys C03 and C09					
f_S	10.18	0.71(0.03)	32.0(3.3)	0.60	0.37
$2f_S$	5.09	0.51(0.03)	21.2(8.5)	0.48	0.19
$3f_S$	3.39	0.17(0.07)	50.0(49.8)	0.11	0.13
Inverted parameters using data from flybys C03, C09, and C10					
f_S	10.18	0.84(0.03)	1.04(1.8)	0.84	0.02
$2f_S$	5.09	0.74(0.04)	0.75(2.0)	0.74	0.01
$3f_S$	3.39	1.03(0.06)	14.1(4.40)	1.03	0.26
$5f_S$	2.04	0.83(0.15)	40.0(14.2)	0.83	0.69

Note. The synodic parameters for the two cases, with associated 3σ confidence intervals, are plotted in the bottom two panels of Figure 7. Note that A_R is the real part of $Ae^{i\phi}$ and A_I is the imaginary part.

where $\hat{\mathbf{m}}_F(t)$ represents the estimated multifrequency amplitude-scaled and phase-delayed driving field portion of the induced magnetic moment,

$$\hat{\mathbf{m}}(t) = \sum_k A_k \mathbf{B}_k \cos\left(2\pi f_k t + \theta_k - \phi_k\right). \tag{10}$$

Here, $\mathbf{B}_k = \sqrt{\mathbf{B}_{R,k}^2 + \mathbf{B}_{I,k}^2}$ and $\theta_k = \arctan(\mathbf{B}_{I,k}/\mathbf{B}_{R,k})$ are the estimated driving field coefficients of Equation 3, $\mathbf{m}_F$ are the estimated induced magnetic moments of each flyby given in Table 3, and F represents the flyby index. The constraints imposed on the solver are $0 < A_k < 1.1$ and $0 < \phi_k < 90$, which are consistent with the bounds of our forward models described previously. In the three flyby case, we use four different frequencies ($f_k = f_S, 2f_S, 3f_S$, and $5f_S$) that best fit the joint data acquired from flybys C03, C09, and C10. We limit the modeling to four discrete frequencies (i.e., eight total induction parameters) because the three-element magnetic moment is different for each of the three flybys, thus limiting the number of parameters that can be solved for. For the two-flyby case (i.e., C03 and C09), we only solve for three frequencies (six total induction parameters) as the three-element magnetic moment for C10 is not considered, thus further limiting the number of parameters that can be solved for.

The extracted amplitude and phase parameters (as well as their 1σ uncertainties) for the two cases are shown in Table 4. Note that the non-monotonic behavior of the estimated amplitude and phase parameters (as a function of period) is not unexpected for various reasons. Although a single conducting layer will respond monotonically as a function of period, a multi-layer body may not due to the screening interaction of induced currents that occurs between multiple layers of varying conductivity and thickness. In the case of Callisto, as the period of the driving wave increases, the wave's interaction transitions from conductive shallower layers (e.g., the ionosphere) to deeper conductive layers (e.g., the ocean). This causes a shift in the primary source of the induced secondary magnetic field (e.g., from ionosphere to ocean), and consequently, the observed phase of the response changes (See Figures S2 and S3 in Supporting Information S1 for amplitude and phase behavior of the forward modeled data set. This was also explained in Cochrane et al. (2021)). Note that because of the relatively high amount of noise in the observations, the uncertainty in the plasma model, and the limited amount of data, the estimated high-order harmonics are not well constrained and therefore not used to assess interior properties of Callisto. However, these high-order harmonics are driven by magnetic waves at frequencies that exhibit much smaller amplitudes, and therefore the accuracy of the reconstructed response is less sensitive to large errors in their estimated values. It is for this reason that we solely use the estimated synodic parameters for the interior assessment of Callisto. In our case, the amplitude of the induction response at the synodic period is estimated to be between 0.80 and 0.88 (3σ), consistent with previous reports and also with the results obtained in the ensemble forward model approach described previously.

The reconstructed signal comprises the induction component, the Jupiter field component, and the scaled plasma component, respectively,

$$\hat{\mathbf{B}}_{SC,F}(t) = \mathbf{D}_F(t)\hat{\mathbf{m}}(t) + \hat{\mathbf{B}}_{J,SC}(t) + C_F\mathbf{B}_{p,F}(t). \tag{11}$$

Thus, given the flyby number F and time t, the total magnetic field measured at the spacecraft can be defined by the parameters A_k, ϕ_k, $\mathbf{B}_k$, θ_k, and C_F. Figure 8 illustrates the reconstructed response $\hat{\mathbf{B}}_{SC,F}(t)$ for the two flyby cases (C03, C09) and three flyby cases (C03, C09, C10), respectively, plotted as dashed black lines, with the raw data $\mathbf{B}_{SC}(t)$ plotted in solid colors (B_x in blue, B_y in red, and B_z in green) for each of the three flybys. As illustrated for both fitting cases, the reconstructed responses for C03 and C09 provide good fits to the observations; however, only the reconstructed response for C10 is additionally closely fit when the data from this flyby are included in the inversion. Therefore, although noisy, the inclusion of C10 provides additional constraints on the underlying induction parameters, thus improving the accuracy of the fit across all three flybys and suggesting an ocean is needed to explain the Galileo observations.

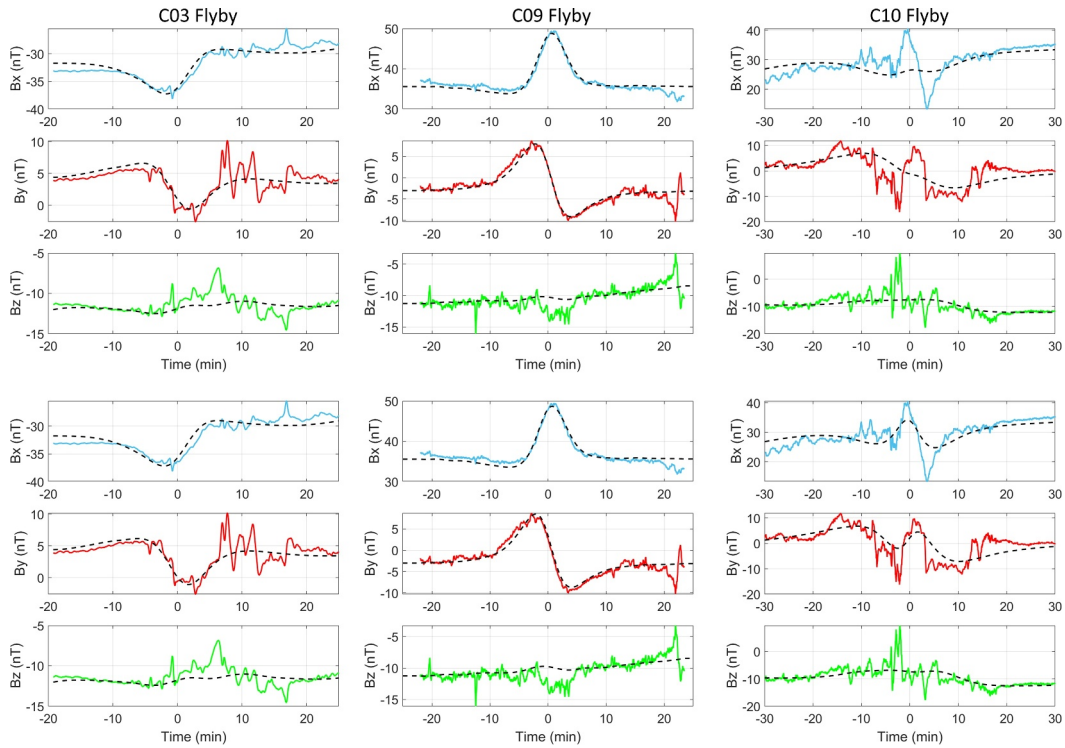

Figure 8. Results obtained from the constrained NLLS inversion. The top row of panels represents the reconstructed data set using the multifrequency model fit from data acquired on flybys C03 and C09 and the bottom row of panels represent the reconstructed data set using the multifrequency model fit from data acquired on flybys C03, C09, and C10. The Galileo data are represented by the solid colored lines (B_x = blue, B_y = red, and B_z = green) and the reconstructed multifrequency model is represented by the dashed black lines. Note the increased accuracy of the fit of flyby C10 when it is retained in the fitting.

5. Discussion

As our results demonstrate, both the inverse and forward modeling approaches support the presence of an ocean when considering data acquired from flyby C10 alongside C03 and C09. However, numerous ocean models with varying characteristics still remain plausible from this analysis. Therefore, we now assess the properties of a subset of the 24,000 models that best fit the modeled observations (within a RMSE of 0.45 nT) from the bottom right panel of Figure 7 (see Section S2 of Supporting Information S1 for more details). Figure 9 depicts the ocean properties associated with the retained best fit forward models for the three-flyby case in the bottom right panel of Figure 7, all separated according to their associated seafloor depths, located at D = 130, 170, 210, 250, 290, and 330 km from the surface. The circles in each plot represent plausible ocean models with specific ocean thickness and conductivity. The inner and outer colors of each circle specify the range (minimum and maximum) of allowable ionospheric HIC. Also plotted in the figure are the distributions of all of the retained models. These distributions indicate that for a given uniformly sampled parameter space (ocean thickness, depth, electrical conductivity, and ionosphere conductance), the best fit models tend to exhibit thicker and deeper oceans. The forward modeled induced magnetic responses associated with all of these models are illustrated in Figure 10. It is clear that these particular ocean models not only agree with the observations made on the C03 and C09 flybys but are also able to produce observations similar to those made on the C10 flyby.

5.1. On the Nature of Plausible Interior Models

Of the many combinations of models considered in this analysis, the best-fit models retained from Figure 9 indicate the presence of an ocean with electrical conductivity in the range 0.5 S/m – 10 S/m. Of this subset of retained models, the models favor thick and deep oceans. A thick ice shell is consistent with Callisto's heavily cratered geology, and has been explained by a modest internal heat transfer through solid-state convection under a fully stagnant lid (McKinnon, 2006). The nominal MoI requires a depth of the seafloor of around 200 km, while the larger depths considered require a lower MoI as permitted in the non-hydrostatic case (Gao &

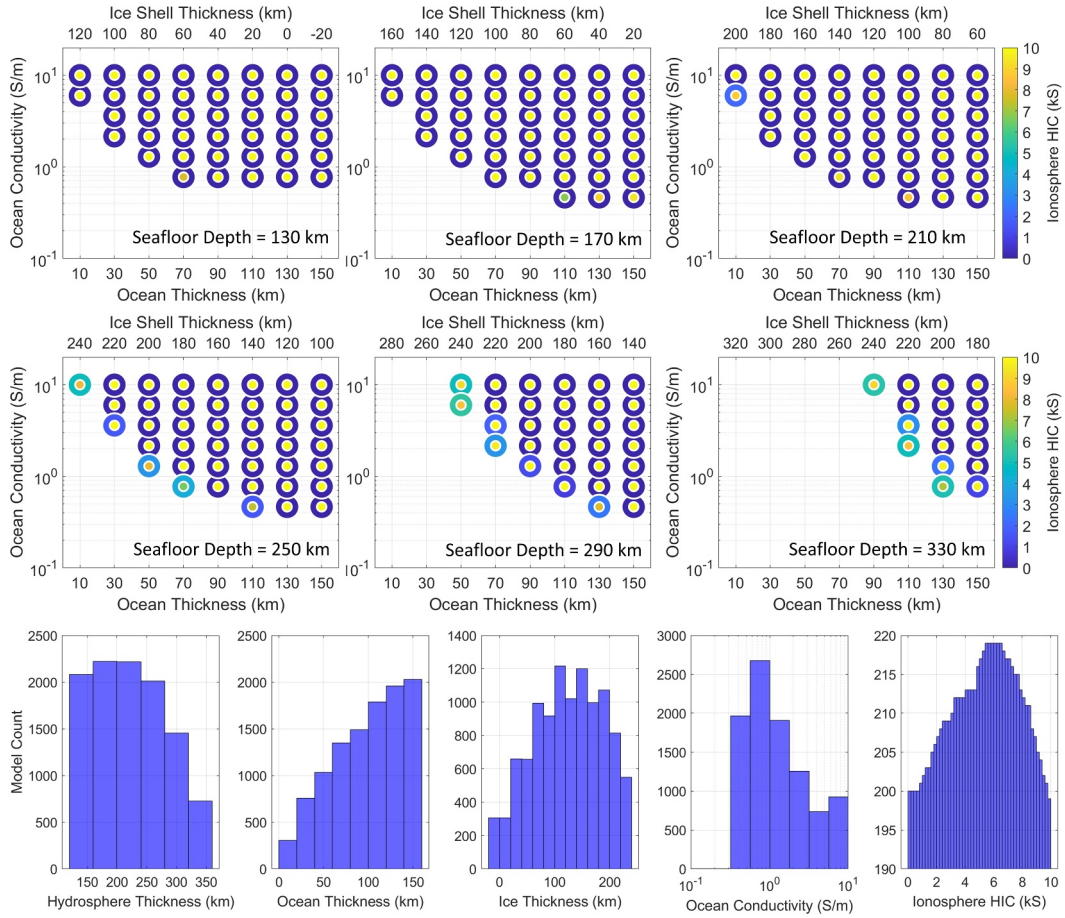

Figure 9. Interior characteristics for best-fit oceans (see associated induced responses in Figure 10) when flybys C03, C09, and C10 are considered. The top six panels represent the subset of models of different seafloor depths measured from the ice shell surface. Plausible combination of ocean thickness, conductivity, and depth, are shown as colored circles, the inner color representing the maximum HIC of the ionosphere and the outer color representing the minimum. The bottom panel of the figure illustrates the distributions of parameters for all best-fit models retained. Although any one of these models is able to explain the measurements, the distributions indicate there are more combinations of thick (e.g., >50 km) and deep (e.g., 150–300 km) oceans that explain the observations.

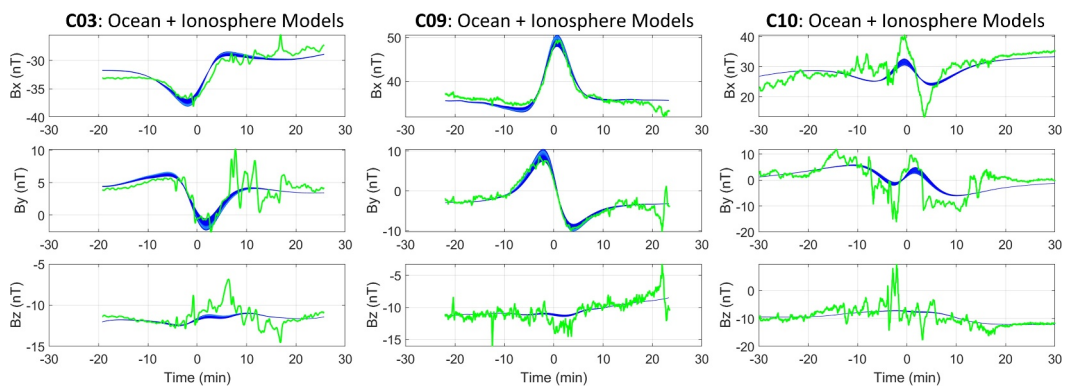

Figure 10. Reconstructed best-fit ocean + ionosphere models captured in Figure 9 for each flyby plotted against the Galileo observations. Note that there were no ionosphere-only models that fit the minimum RMSE criteria threshold.

Stevenson, 2013; Styczinski, Vance, & Melwani Daswani, 2023; Vance et al., 2018). Furthermore, in each thin ocean case, the fit corresponds to a narrow range of ionospheric HIC, which decreases the likelihood that this solution is true in the statistical sense.

The prevalence of models in the solution space with thicker oceans suggests sustained heating in addition to the dominant long-lived radiogenic sources. Assuming no tidal heating and heat transfer via conduction, thermal evolution modeling indicates that Callisto should hold a deep ocean no thicker than 70 km at present for a CI-chondrite-like inventory of radioisotopes (see Section S3 of Supporting Information S1 for thermal modeling methodology). Tidal heating from eccentricity tides for Callisto's current orbital distance and small eccentricity (0.0074) is small, at least one order of magnitude less than radiogenic heating (Chen et al., 2014). Hence, the best-fit interior models with thicker oceans could point to the contribution of a recent episode of tidal heating from obliquity-driven tides, as suggested by Downey et al. (2020).

Cosmochemical considerations may help to further constrain the space of best-fit models. For an ocean composition determined by the aqueous alteration of a chondritic composition at 1 bar, the electrical conductivity would only be up to 0.2 S/m (for a temperature of 5°C, Castillo-Rogez et al., 2022). The main solute in that case would likely be dissolved NaCl, as found on the surface of Europa (Trumbo et al., 2019). Electrical conductivity is further reduced at high pressures (100s of MPa) and reduced temperature in Callisto's ocean (Pan et al., 2021; Vance et al., 2021). Hence, the contribution of additional solutes, such as ammonium, carbonate, and bicarbonate ions, may be required to explain the inferred electrical conductivity range 0.5 S/m – 10 S/m (Castillo-Rogez et al., 2022). A high concentration of carbonates is supported by the detection of CO_2 on Callisto (e.g., Hibbitts et al., 2002). Furthermore, infrared absorption features measured by the Juno spacecraft at Ganymede are consistent with the presence of carbonates (and ammonium-bearing salts, Tosi et al., 2023). Hence, it is plausible that these compounds could also be present in Callisto's ocean. However, the lack of experimental data on the electrical conductivity of NaCl- and carbonate-rich solutions at relevant pressures and temperatures prevents the narrowing of a salinity range.

5.2. Effects of Asymmetry in Callisto's Ionosphere

Our analysis thus far has primarily focused on the spherical symmetry of the ocean and ionosphere; however, the asymmetric effects are worth commenting on. Photoionization is expected to be the dominant process supporting Callisto's ionosphere (Cunningham et al., 2015), so a day—night dichotomy is likely present (Hartkorn et al., 2017). However, a recent study by Carberry Mogan, Johnson, et al. (2023) estimated the electron impact ionization rate to be comparable to the photoionization rate at Callisto, at least when the moon is embedded within the jovian magnetospheric plasma sheet. Further investigation is required to determine the precipitation pattern and the energy deposition rate of these thermal electrons into Callisto's atmosphere to determine their ionization patterns (Carberry Mogan, Liuzzo, et al., 2023). However, if the resultant induction signal from such an asymmetric ionosphere indeed contains significant contributions from ionospheric conductivity (Hartkorn & Saur, 2017; Liuzzo et al., 2017), then an asymmetric ionospheric profile could result in additional high-order magnetic moments atop of the induced dipole moment that results from the spherically symmetric conducting layers (Styczinski et al., 2022).

For each of the C03, C09, and C10 flybys, we examined the effects of ionospheric asymmetry for two different models, Model 1 and Model 2, that have magnetic responses similar to the best-fit models retained in the two-flyby and three-flyby cases, respectively. Model 1 exhibits a synodic amplitude response of 0.64 and phase delay of 40.2° (corresponding to an ocean with thickness of 70 km, conductivity of 0.1 S/m, seafloor depth of 290 km, and ionosphere HIC of 1268 S) and Model 2 exhibits a synodic amplitude response of 0.81 and phase delay of 3.6° (corresponding to an ocean with thickness of 110 km, conductivity of 3.6 S/m, seafloor depth of 260 km, and ionosphere HIC of 2284 S). We modeled the contributions from asymmetry based on a simple parameterization for Callisto's ionosphere, as described by Styczinski et al. (2022) after Hartkorn et al. (2017). To model the asymmetric ionosphere, we assume a near-spherical layer with constant Pedersen conductivity, with a bulge up to ∼185 km at the subsolar point and a depression down to ∼15 km on the night side (as in Styczinski et al., 2022). Here, the Sun direction was used to orient the day–night asymmetry for each fly and the induced magnetic field was evaluated with *MoonMag* (Styczinski, 2024) for both Model 1 and Model 2 at the time of closest approach for each flyby using the excitations from Jupiter listed in Table 1.

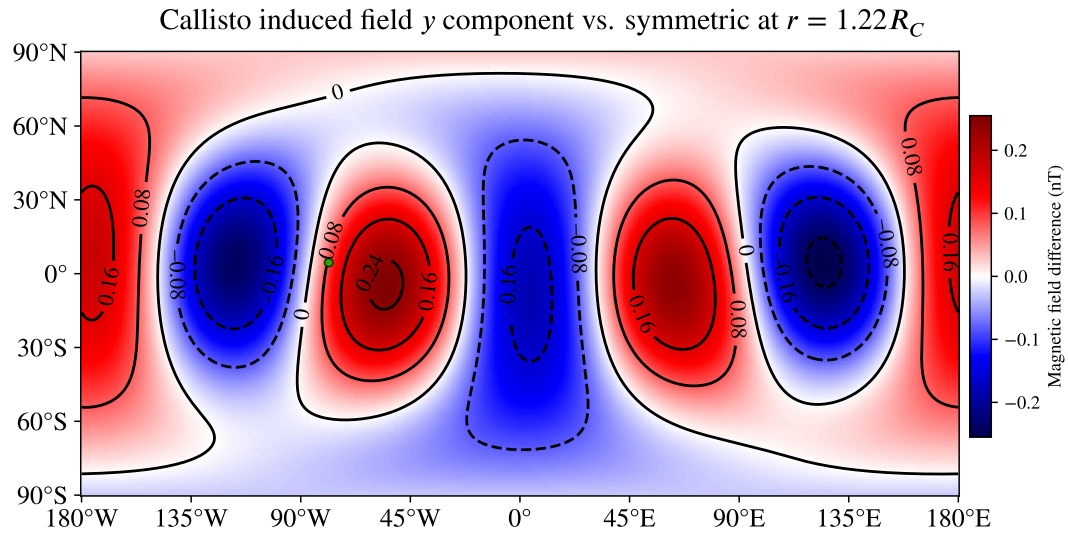

Figure 11. The magnetic effects of Callisto's asymmetric ionosphere. This figure illustrates the difference between the IAU y component of the induced magnetic field from Model 2, described in the text, for a spherically symmetric and asymmetric ionosphere, both evaluated at the instant of closest approach for the C10 encounter. The altitude of Galileo at closest approach of Callisto on flyby C10 is 527 km and marked with a circle near 0° latitude and 90° W longitude. Differences in the x component are nearly the same but with a different spatial orientation, and differences in the z component are about 2/3 as great, but negligible in the equatorial plane where most flybys occurred. Evaluated with *MoonMag* (Styczinski, 2024).

The largest differences observed in the induction response for the asymmetric case was for Model 1 on the C10 flyby, where each component exhibited a perturbation of the induction field by as much as 1.5 nT at closest approach. The differences in magnetic field from Model 1 for the other two flybys were smaller, up to about 0.25 nT for C03 and 0.8 nT for C09. Model 2 on the other hand only exhibited a maximum difference in field of about 0.25 nT for flyby C10, illustrated in Figure 11, and even smaller for the other two flybys. The degree of influence from asymmetry in the ionosphere is dictated by the conductivity of both the ocean and the ionosphere. Regions of the parameter space with greater ionospheric HIC and lower ocean conductivity will be most affected by this asymmetry, contributing systematic uncertainties on the order of 0.1 nT – 3 nT. Together, this analysis suggests that future work involving induction in Callisto's ionosphere must account for any expected asymmetry in order to interpret the measurements—the differences we calculate represent as much as half the magnitude of the induced field for some latitudes and longitudes.

6. Conclusion

We have demonstrated the application of combined inverse and ensemble forward modeling to derive further insights into Callisto's interior from the limited Galileo magnetometer data set. Our analysis, the first to simultaneously fit C03, C09, and C10 flyby data together, favors the presence of a thick and deep ocean within Callisto. It is challenging to place tighter constraints on the properties of Callisto's ocean because of the limited number of close Galileo flybys that produced reliable data and because of the uncertainty associated with the plasma interaction. However, measurements that will be acquired in the future should make it possible to confirm and characterize the ocean. NASA's Europa Clipper mission, successfully launched on 14 October 2024, is scheduled to make nine flybys of Callisto (seven within 1800 km of the surface, four of those within 250 km) in years 2032 and 2033 where its magnetometer (ECM; Kivelson et al., 2023) will operate continuously. Additionally, the baseline tour for ESA's JUICE mission is scheduled to perform 21 flybys of Callisto (Cappuccio et al., 2022), all within 7000 km of the surface and most below 1000 km. Together, these missions should produce a joint magnetic induction data set that encompasses a wide range of JS3 longitudes and Callisto's true anomaly phases. Additionally, the plasma instrument for magnetic sounding on Europa Clipper (PIMS; Westlake et al., 2023) and the Particle Environment Package (PEP) and Radio and Plasma Wave Investigation (RWPI) instruments on JUICE will enable accurate measurement of the plasma environment (Galli et al., 2022), supporting improved modeling of the plasma field contribution in magnetometer measurements. These flybys will also allow for a confident

independent interpretation of the interior density structure through gravity science and altimetry (Cappuccio et al., 2022; Mazarico et al., 2023; Roberts et al., 2023).

Conflict of Interest

The authors declare no conflicts of interest relevant to this study.

Data Availability Statement

The data contained in this publication are archived on Zenodo and publicly accessible with https://doi.org/10.5281/zenodo.14434831 (Cochrane, 2024). The data are stored in Matlab.mat structure files with an associated.m script for easy data extraction and figure generation. For all timing and ephemeris computation in this work, the NAIF developed SPICE toolkit (Acton et al., 2018) for Matlab called mice was utilized, freely available at naif.jpl.nasa.gov/naif. All magnetic field models and field line visuals were implemented in MATLAB. The most recent kernel files were leveraged and all IAU defined reference frames defined in the IAU working group report (Archinal et al., 2018) were used.

Acknowledgments

The authors thank Krishan Khurana and Margy Kivelson of UCLA and Xianzhe Jia of the University of Michigan for the fruitful discussions that were had over the years on magnetic induction and plasma interaction at Europa, which were very insightful for the methods developed in this work. This work was carried out at the Jet Propulsion Laboratory, California Institute of Technology, under a contract with NASA (80NM0018D0004). Partial funding support was provided by the NASA Discovery Program, as part of the Trident Mission Concept Phase A study (80NM0020F0034), to develop methods capable of detecting oceans in icy bodies with conductive ionospheres like Triton and also analogs like Callisto where real data exists. Additional funding support was provided internally from JPL's Office of Research and Development. Some work by M.J.S. was supported by an appointment to the NASA Postdoctoral Program at the Jet Propulsion Laboratory, California Institute of Technology, administered by Oak Ridge Associated Universities under a contract with NASA (80HQTR21CA005). L. L. acknowledges support from NASA Solar System Workings Grant 80NSSC21K0152. C. J. C., S. D. V., and J. C. C.-R. recognize support from NASA Precursor Science Investigations for Europa Grant 22-PSIE22_2–0024. Some data used in this work were generated using open source software frameworks *PlanetProfile* (Vance et al., 2021), *SeaFreeze* (Journaux et al., 2024), *PlanetMag* (Cochrane & Styczinski, 2024), and *MoonMag* (Styczinski, 2024).

References

Acton, C., Bachman, N., Semenov, B., & Wright, E. (2018). A look towards the future in the handling of space science mission geometry. *Planetary and Space Science*, *150*, 9–12. (Enabling Open and Interoperable Access to Planetary Science and Heliophysics Databases and Tools). https://doi.org/10.1016/j.pss.2017.02.013

Archinal, B. A., Acton, C. H., A'Hearn, M. F., Conrad, A., Consolmagno, G. J., Duxbury, T., et al. (2018). Report of the IAU working group on cartographic coordinates and rotational elements: 2015. *Celestial Mechanics and Dynamical Astronomy*, *130*(3), 22. https://doi.org/10.1007/s10569-017-9805-5

Biersteker, J. B., Weiss, B. P., Cochrane, C. J., Harris, C. D., Jia, X., Khurana, K. K., et al. (2023). Revealing the interior structure of icy moons with a Bayesian approach to magnetic induction measurements. *Planetary Science Journal*, *4*(4), 62. https://doi.org/10.3847/PSJ/acc331

Cappuccio, P., Di Benedetto, M., Durante, D., & Iess, L. (2022). Callisto and Europa gravity measurements from JUICE 3GM experiment simulation. *The Planetary Science Journal*, *3*(8), 199. https://doi.org/10.3847/psj/ac83c4

Carberry Mogan, S. R., Johnson, R. E., Vorburger, A., & Roth, L. (2023). Electron impact ionization in the icy Galilean satellites' atmospheres. *The European Physical Journal D*, *77*(2), 26. https://doi.org/10.1140/epjd/s10053-023-00606-8

Carberry Mogan, S. R., Liuzzo, L., Poppe, A. R., Simon, S., Szalay, J. R., Tucker, O. J., & Johnson, R. E. (2023). Callisto's atmosphere: The oxygen enigma. *Journal of Geophysical Research: Planets*, *128*(9), e2023JE007894. https://doi.org/10.1029/2023JE007894

Castillo-Rogez, J. C., Daswani, M. M., Glein, C. R., Vance, S. D., & Cochrane, C. J. (2022). Contribution of non-water ices to salinity and electrical conductivity in ocean worlds. *Geophysical Research Letters*, *49*(16), e2021GL097256. https://doi.org/10.1029/2021GL097256

Chen, E., Nimmo, F., & Glatzmaier, G. A. (2014). Tidal heating in icy satellite oceans. *Icarus*, *229*, 11–30. https://doi.org/10.1016/j.icarus.2013.10.024

Cochrane, C. J. (2024). Reanalysis of Galileo magnetometer data at Callisto [Dataset, Software]. *Zenodo*. https://doi.org/10.5281/zenodo.13242120

Cochrane, C. J., Persinger, R. R., Vance, S. D., Midkiff, E. L., Castillo-Rogez, J., Luspay-Kuti, A., et al. (2022). Single-and multi-pass magnetometric subsurface ocean detection and characterization in icy worlds using Principal Component Analysis (PCA): Application to Triton. *Earth and Space Science*, *9*(2), e2021EA002034. https://doi.org/10.1029/2021EA002034

Cochrane, C. J., & Styczinski, M. J. (2024). Planetmag [Software]. https://coreyjcochrane.github.io/PlanetMag/.GitHub

Cochrane, C. J., Vance, S. D., Biersteker, J. B., Styczinski, M. J., & Weiss, B. (2024). On detecting and characterizing planetary oceans in the solar system using a distance-based ensemble modelling approach: Application to the Uranus system. *Philosophical Transactions of the Royal Society A: Mathematical, Physical & Engineering Sciences*, *382*(2286), 20240086. https://doi.org/10.1098/rsta.2024.0086

Cochrane, C. J., Vance, S. D., Nordheim, T. A., Styczinski, M. J., Masters, A., & Regoli, L. H. (2021). In search of subsurface oceans within the uranian moons. *Journal of Geophysical Research: Planets*, *126*(12), e2021JE006956. https://doi.org/10.1029/2021JE006956

Connerney, J. E. P., Timmins, S., Herceg, M., & Joergensen, J. L. (2020). A Jovian magnetodisc model for the Juno era. *Journal of Geophysical Research: Space Physics*, *125*(10). https://doi.org/10.1029/2020ja028138

Cunningham, N. J., Spencer, J. R., Feldman, P. D., Strobel, D. F., France, K., & Osterman, S. N. (2015). Detection of Callisto's oxygen atmosphere with the hubble space telescope. *Icarus*, *254*, 178–189. https://doi.org/10.1016/j.icarus.2015.03.021

Downey, B. G., Nimmo, F., & Matsuyama, I. (2020). Inclination damping on Callisto. *Monthly Notices of the Royal Astronomical Society*, *499*(1), 40–51. https://doi.org/10.1093/mnras/staa2802

Eckhardt, D. H. (1963). Geomagnetic induction in a concentrically stratified Earth. *Journal of Geophysical Research*, *68*(23), 6273–6278. https://doi.org/10.1029/JZ068i023p06273

Galli, A., Vorburger, A., Carberry Mogan, S. R., Roussos, E., Stenberg Wieser, G., Wurz, P., et al. (2022). Callisto's atmosphere and its space environment: Prospects for the particle environment package on board JUICE. *Earth and Space Science*, *9*(5). https://doi.org/10.1029/2021ea002172

Gao, P., & Stevenson, D. J. (2013). Nonhydrostatic effects and the determination of icy satellites' moment of inertia. *Icarus*, *226*(2), 1185–1191. https://doi.org/10.1016/j.icarus.2013.07.034

Hartkorn, O., & Saur, J. (2017). Induction signals from Callisto's ionosphere and their implications on a possible subsurface ocean. *Journal of Geophysical Research: Space Physics*, *122*(11), 11–677. https://doi.org/10.1002/2017JA024269

Hartkorn, O., Saur, J., & Strobel, D. F. (2017). Structure and density of Callisto's atmosphere from a fluid-kinetic model of its ionosphere: Comparison with Hubble Space Telescope and Galileo observations. *Icarus*, *282*, 237–259. https://doi.org/10.1016/j.icarus.2016.09.020

Hibbitts, C. A., Klemaszewski, J. E., McCord, T. B., Hansen, G. B., & Greeley, R. (2002). CO_2-rich impact craters on Callisto. *Journal of Geophysical Research*, *107*(E10), 14-1–14-12. https://doi.org/10.1029/2000JE001412

Journaux, B., Brown, J. M., Espinoza, P., Jones, U., Clinton, E., Gordon, T., & Powell-Palm, M. J. (2024). Bjournaux/SeaFreeze: Updated package README and authorship info [Software]. https://github.com/Bjournaux/SeaFreeze

Khurana, K. K. (1997). Euler potential models of Jupiter's magnetospheric field. *Journal of Geophysical Research*, *102*(A6), 11295–11306. https://doi.org/10.1029/97JA00563

Khurana, K. K., Kivelson, M. G., & Russell, C. T. (2002). Searching for liquid water in Europa by using surface observatories. *Astrobiology*, *2*(1), 93–103. https://doi.org/10.1089/153110702753621376

Khurana, K. K., Kivelson, M. G., Stevenson, D. J., Schubert, G., Russell, C. T., Walker, R. J., & Polanskey, C. (1998). Induced magnetic fields as evidence for subsurface oceans in Europa and Callisto. *Nature*, *395*(6704), 777–780. https://doi.org/10.1038/27394

Kivelson, M. G., Jia, X., Lee, K. A., Raymond, C. A., Khurana, K. K., Perley, M. O., et al. (2023). The Europa clipper magnetometer. *Space Science Reviews*, *219*(48), 48. https://doi.org/10.1007/s11214-023-00989-5

Kivelson, M. G., Khurana, K. K., Stevenson, D. J., Bennett, L., Joy, S., Russell, C. T., et al. (1999). Europa and Callisto: Induced or intrinsic fields in a periodically varying plasma environment. *Journal of Geophysical Research*, *104*(A3), 4609–4625. https://doi.org/10.1029/1998JA900095

Liuzzo, L., Feyerabend, M., Simon, S., & Motschmann, U. (2015). The impact of Callisto's atmosphere on its plasma interaction with the Jovian magnetosphere. *Journal of Geophysical Research: Space Physics*, *120*(11), 9401–9427. https://doi.org/10.1002/2015JA021792

Liuzzo, L., Simon, S., & Feyerabend, M. (2018). Observability of Callisto's inductive signature during the JUpiter ICy moons Explorer mission. *Journal of Geophysical Research: Space Physics*, *123*(11), 9045–9054. https://doi.org/10.1029/2018JA025951

Liuzzo, L., Simon, S., Feyerabend, M., & Motschmann, U. (2016). Disentangling plasma interaction and induction signatures at Callisto: The Galileo C10 flyby. *Journal of Geophysical Research: Space Physics*, *121*(9), 8677–8694. https://doi.org/10.1002/2016JA023236

Liuzzo, L., Simon, S., Feyerabend, M., & Motschmann, U. (2017). Magnetic signatures of plasma interaction and induction at Callisto: The Galileo C21, C22, C23, and C30 flybys. *Journal of Geophysical Research: Space Physics*, *122*(7), 7364–7386. https://doi.org/10.1002/2017JA024303

Mazarico, E., Buccino, D., Castillo-Rogez, J., Dombard, A. J., Genova, A., Hussmann, H., et al. (2023). The Europa clipper gravity and radio science investigation. *Space Science Reviews*, *219*(4), 30. https://doi.org/10.1007/s11214-023-00972-0

McKinnon, W. B. (2006). On convection in ice I shells of outer solar system bodies, with detailed application to Callisto. *Icarus*, *183*(2), 435–450. https://doi.org/10.1016/j.icarus.2006.03.004

Müller, J., Simon, S., Motschmann, U., Schüle, J., Glassmeier, K.-H., & Pringle, G. J. (2011). A.I.K.E.F.: Adaptive hybrid model for space plasma simulations. *Computer Physics Communications*, *182*(4), 946–966. https://doi.org/10.1016/j.cpc.2010.12.033

Neubauer, F. M. (1999). Alfvén wings and electromagnetic induction in the interiors: Europa and Callisto. *Journal of Geophysical Research*, *104*(A12), 28671–28684. https://doi.org/10.1029/1999JA900217

Pan, Y., Yong, W., & Secco, R. A. (2021). Electrical conductivity of aqueous NaCl at high pressure and low temperature: Application to deep subsurface oceans of icy moons. *Geophysical Research Letters*, *48*(17), e2021GL094020. https://doi.org/10.1029/2021GL094020

Roberts, J. H., McKinnon, W. B., Elder, C. M., Tobie, G., Biersteker, J. B., Young, D., et al. (2023). Exploring the interior of Europa with the Europa Clipper. *Space Science Reviews*, *219*(6), 46. https://doi.org/10.1007/s11214-023-00990-y

Seufert, M., Saur, J., & Neubauer, F. M. (2011). Multi-frequency electromagnetic sounding of the Galilean moons. *Icarus*, *214*(2), 477–494. https://doi.org/10.1016/j.icarus.2011.03.017

Srivastava, S. P. (1966). Theory of the magnetotelluric method for a spherical conductor. *Geophysical Journal International*, *11*(4), 373–387. https://doi.org/10.1111/j.1365-246X.1966.tb03090.x

Styczinski, M. J. (2024). itsmoosh/MoonMag [Software]. *Zenodo*. https://doi.org/10.5281/zenodo.5002955

Styczinski, M. J., & Cochrane, C. J. (2024). Planetmag: Software for evaluation of outer planet magnetic fields and corresponding excitations at their moons. *Earth and Space Science*, *11*(6). https://doi.org/10.1029/2024EA003552

Styczinski, M. J., Vance, S. D., Harnett, E. M., & Cochrane, C. J. (2022). A perturbation method for evaluating the magnetic field induced from an arbitrary, asymmetric ocean world analytically. *Icarus*, *376*(1), 114840. https://doi.org/10.1016/j.icarus.2021.114840

Styczinski, M. J., Vance, S. D., & Melwani Daswani, M. (2023). *PlanetProfile:* Self-consistent interior structure modeling for terrestrial bodies in python. *Earth and Space Science*, *10*(8), e2022EA002748. https://doi.org/10.1029/2022EA002748

Styczinski, M. J., Vance, S. D., Niesyt, M., Lisitsyn, A., Daswani, M. M., Marusiak, A. G., et al. (2023). vancesteven/PlanetProfile [Software]. *Zenodo*. https://doi.org/10.5281/zenodo.844130

Tosi, F., Mura, A., Cofano, A., Zambon, F., Glein, C. R., Ciarniello, M., et al. (2023). Salts and organics on Ganymede's surface observed by the JIRAM spectrometer onboard Juno. *Nature Astronomy*, *8*, 1–12. https://doi.org/10.1038/s41550-023-02107-5

Trumbo, S. K., Brown, M. E., & Hand, K. P. (2019). Sodium chloride on the surface of Europa. *Science Advances*, *5*(6), eaaw7123. https://doi.org/10.1126/sciadv.aaw7123

Vance, S. D., Panning, M. P., Stähler, S., Cammarano, F., Bills, B. G., Tobie, G., et al. (2018). Geophysical investigations of habitability in ice-covered ocean worlds. *Journal of Geophysical Research: Planets*, *123*(1), 180–205. https://doi.org/10.1002/2017JE005341

Vance, S. D., Styczinski, M. J., Bills, B. G., Cochrane, C. J., Soderlund, K. M., Gómez-Pérez, N., & Paty, C. (2021). Magnetic induction responses of Jupiter's ocean moons including effects from adiabatic convection. *Journal of Geophysical Research: Planets*, *126*(2), e2020JE006418. https://doi.org/10.1029/2020JE006418

Westlake, J. H., Jr, R. L. M., Grey, M., Coren, D., Rymer, A. M., Cochrane, C. J., et al. (2023). The plasma instrument for magnetic sounding (PIMS) on the Europa clipper mission. *Space Science Reviews*, *219*(62), 62. https://doi.org/10.1007/s11214-023-01002-9

Zimmer, C., Khurana, K. K., & Kivelson, M. G. (2000). Subsurface oceans on Europa and Callisto: Constraints from galileo magnetometer observations. *Icarus*, *147*(2), 329–347. https://doi.org/10.1006/icar.2000.6456

References From the Supporting Information

Canup, R. M., & Ward, W. R. (2002). Formation of the Galilean satellites: Conditions of accretion. *Astronomical Journal*, *124*(6), 3404–3423. https://doi.org/10.1086/344684

Castillo-Rogez, J. C., & Lunine, J. I. (2010). Evolution of Titan's rocky core constrained by Cassini observations. *Geophysical Research Letters*, *37*(20). https://doi.org/10.1029/2010GL044398

Néri, A., Guyot, F., Reynard, B., & Sotin, C. (2020). A carbonaceous chondrite and cometary origin for icy moons of Jupiter and Saturn. *Earth and Planetary Science Letters*, *530*, 115920. https://doi.org/10.1016/j.epsl.2019.115920

Verma, A., Khurana, K., Walker, R., & Margot, J.-L. (2022). Vertical structure of the Callisto ionosphere from Galileo radio occultation data and its implication on the moon's interior. *Authorea Preprints*.